

Floquet stability analyses of oscillating boundary layers on adiabatic slopes

Bryan E. Kaiser¹†, Lawrence J. Pratt²

¹Los Alamos National Laboratory, Los Alamos, NM, USA

²Woods Hole Oceanographic Institution, Woods Hole, MA, USA

(Received xx; revised xx; accepted xx)

The presence of a no-slip, impermeable, adiabatic, sloped boundary in an otherwise quiescent, stably stratified, Boussinesq flow generates baroclinic vorticity within a diffusive boundary layer. Such conditions are typical of the oscillating boundary layers on adiabatic abyssal slopes, sloped lake bathymetry, and sloped coastal bathymetry in the absence of high-wavenumber internal waves, mean flows, far-field turbulence on larger scales, and resonant tidal-bathymetric interaction. We investigate the linear stability of the oscillating flow within non-dimensional parameter space typical of the M_2 tide and hydraulically smooth, mid-latitude abyssal slopes through Floquet linear stability analysis. The flow dynamics depend on three non-dimensional variables: the Reynolds number for Stokes' second problem (Re), the Prandtl number, and a frequency ratio that accounts for the resonance conditions (C , criticality) of the buoyant restoring force and the tidal forcing. The Floquet analysis results suggest that oscillating laminar boundary layers on adiabatic abyssal slopes are increasingly unstable as Reynolds number, criticality parameter, and/or spanwise disturbance wavenumber are increased. We also show that the two-dimensional Floquet linear instability necessarily generates three-dimensional baroclinic vorticity, which suggests that the evolution of the gravitational instabilities may be nonlinear as $t \rightarrow \infty$.

1. Introduction

The dynamics of oscillating stratified boundary layers on sloping bathymetry may be an important mechanism of diapycnal water mass transformation in the context of the global overturning circulation of the ocean (Ferrari *et al.* (2016)). A fundamental understanding of the dynamical pathways between laminar, transitional, and turbulent states is lacking. Historically, analyses of turbulent flows begin by answering the questions: how stable is the flow to linear disturbances, what are the relevant mechanisms of linear instability, and how does disturbance growth change as a function of the relevant non-dimensional parameters (Trefethen *et al.* (1993))? We examine the linear stability of the laminar boundary layers that form as internal waves heave isopycnals up and down infinite slopes to answer these questions for oscillating stratified boundary layers on sloping bathymetry. Our use of a semi-infinite, constant slope model is justified by the large separation of length scales between the viscous lengthscale of the laminar boundary layers, $\mathcal{O}(1)$ cm, and the internal-wave-generative abyssal slope length scales of $\mathcal{O}(10)$ km (Jayne & St. Laurent (2001), Goff & Arbic (2010)). The geometry and scales that are typical of these boundary layers are illustrated by Figure 1.

In the absence of shear, gravitational instabilities are often linear instabilities as is

† Email address for correspondence: bkaiser@lanl.gov

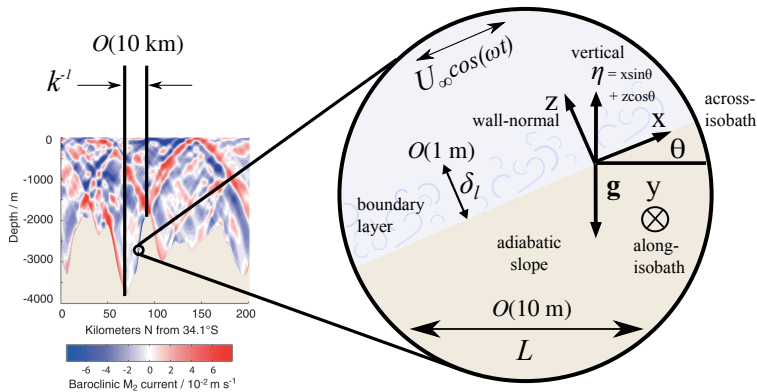


FIGURE 1. Illustration of Boussinesq boundary layers on abyssal slopes arising from the heaving of density surfaces up and down slope by internal waves with wavelengths $O(10)$ km. The M_2 tide velocity contour plot on the left is from Zilberman *et al.* (2009).

the case for Rayleigh-Taylor and Rayleigh-Benard instabilities. In sheared, gravitationally unstable flows, the transition pathways can be more complicated. Theoretical and experimental evidence suggest that two dimensional rolls, initiated by linear near-wall gravitational instabilities and subsequently sheared into bursts of three-dimensional turbulence, are the dominant transition-to-turbulence mechanism in gravitationally unstable Couette flow (Bénard & Avsec (1938), Chandra (1938), Brunt (1951), Deardorff (1965), Gallagher & A. Mercer (1965), Ingersoll (1966)). Recently similar mechanisms have been observed in DNS data of oscillating Boussinesq boundary layers on adiabatic sloping boundaries, which are a potentially important regime in the context of abyssal water mass transformation (Kaiser (2020)). In this article, the linear stability of the non-rotating boundary layers is calculated to determine if the gravitational instability is a significant linear instability across a much broader region of parameter space than can be sampled by direct numerical simulations.

The linear stability of stationary flows is conventionally analyzed by introducing infinitesimal disturbances to the flow and linearizing the governing equations about the stationary base flow to form governing equations for the growth or decay of the infinitesimal disturbances (Trefethen *et al.* (1993)). However, the disturbance equations for oscillating base flows contain time-periodic coefficients and, therefore, conventional eigenvalue methods for analyzing the linear growth or decay of disturbances cannot be applied to oscillatory flows. Instead, the linear stability is determined by applying instantaneous instability theory (IIT) or Floquet global instability theory (Luo & Wu (2010)).

IIT is the *ad hoc* application of conventional linear instability theory to examine the stability of the base flow at a discrete time (Von Kerczek & Davis (1976)). For example, in the case of Stokes' second problem (SSP, sometimes referred to as Stokes layers in the literature), the Orr-Sommerfeld equation is solved for the growth rates of disturbances to base flow at a chosen instant in the period. To evaluate the global stability, or stability over the entire period, the instantaneous stability calculation must be performed over many instants within the period. If one or more instantaneous modes exhibit positive growth rates throughout the period, then the flow is globally unstable according to IIT Luo & Wu (2010). However, the validity of the IIT approach rests on the assumption that the instantaneous growth rates are much larger than the frequency of the base flow, i.e. the quasi-steady flow assumption. IIT is justifiable for the stability calculations for

high Reynolds number, constant density flows because the instantaneous growth rates increase as a function of Reynolds number (Dwoyer & Hussaini (1987)). However, low- to moderate-Reynolds number Stokes layer calculations by Luo & Wu (2010) showed that global stability estimates from IIT, which by definition fail to represent linear energy exchanges between instantaneous modes, are not predictive of linear global instabilities.

Floquet instability theory (Floquet (1883)) pertains to the net growth or suppression of instabilities over the course of one period. All periodic instantaneous globally unstable modes are unstable Floquet modes (Luo & Wu (2010), Dwoyer & Hussaini (1987)), but the opposite is not true: an unstable Floquet mode can correspond to linear energy exchange between two or more instantaneous modes that do not produce IIT global stability. Therefore, the evolution of a Floquet mode over a period does not necessarily correspond to the evolution of an instantaneous instability that occurs during that period, but it does represent the global effect of linear instantaneous instabilities.

In this Article, we examine gravitational instabilities in laminar oscillating flow on adiabatic slopes in which the oscillatory forcing is oriented in the across-isobath direction for parameter regimes typical of super-inertial dynamics in abyssal ocean at low- to mid-latitudes. First, we discuss Floquet analysis of tensors, and, second, we define the Floquet stability problem. Third, we discuss a simple numerical method, and then we discuss the neutral stability curves over a broad range of subcritical and supercritical slopes before concluding.

2. Problem formulation

Even in the absence of an oscillatory body force, motion arises in Boussinesq diffusive boundary layers on adiabatic sloping boundaries because baroclinic vorticity is created by the tilting density surfaces parallel to the wall normal axis, such that the angle θ separates density surfaces from the hydrostatic pressure gradient in the vertical within the diffusive boundary layer (see Figure 2). The baroclinic vorticity is oriented in the along-slope, constant isobath direction (y axis in Figure 2), which drives across-slope wall parallel flows with a net upslope transport. Phillips (1970) and Wunsch (1970) simultaneously derived analytical solutions for these laminar flows that were validated by the laboratory experiments of Peacock *et al.* (2004).

The addition of an oscillating body force in the across-slope direction (x axis in Figure 2) gives rise to a class of boundary layers that, in various limits, collapse to familiar classical oscillating boundary layers (e.g. Stokes' second problem if the stratification vanishes, Stokes-Ekman layers in a rotating reference frame, Stokes-buoyancy layers if $\theta = \pi/2$, etc) and it is representative of the frictional interaction of low-mode extra-critical baroclinic tidal flows in the ocean. Baidulov (2010) derived the linear solutions for the oscillating, stratified, viscous, and diffusive boundary layer in a stationary (not rotating) reference frame (hereafter the oscillating boundary layer, OBL) and found that the linear flow is a superposition of two evanescent modes. Baidulov (2010) noted that the phase of one of the boundary layer modes changes sign as the slope increases from subcritical to supercritical, where critical slope is defined by the slope angle θ_c that satisfies $\omega = N \sin \theta_c$ and N is the buoyancy frequency. The criticality parameter, defined by dimensional analysis of the governing equations, is

$$C = \frac{N \sin \theta}{\omega}, \quad (2.1)$$

where if $\theta = \theta_c$ then $C = 1$ and subcritical and supercritical slopes can be defined as $C < 1$ and $C > 1$, respectively. The change in sign of the boundary layer solution mode

indicates that the boundary layers share some of the dynamics of the parent flow (i.e. the larger scale internal wave field in the oceanic example), which undergoes a change of sign of the group velocity of the radiated or reflected internal waves as the slope angle increases from subcritical to supercritical topography. At critical slope, the OBL and the far field flow resonate because the frequency of buoyant restoring force parallel matches that of the across-isobath velocity oscillation.

A commonly observed OBL flow feature is the formation and growth of gravitational instabilities produced by the upslope advection of relatively heavy water over relatively light water trapped at the boundary by friction. The energy source for OBL gravitational instabilities is the baroclinic tide, the same as for near boundary gravitational instabilities and overturning formed by critically reflecting internal waves (Dauxois & Young (1999)) and the nonlinear baroclinic tide generation at critical slope (Rapaka *et al.* (2013), Gayen & Sarkar (2011), Sarkar & Scotti (2017)). However, gravitational instabilities at critical slope are formed by primarily inviscid nonlinearities in the baroclinic response to the barotropic tide (Dauxois & Young (1999)); whereas, the OBL gravitational instabilities are formed by viscous, insulating boundary conditions (Hart (1971)). OBL gravitational instabilities on extra-critical slopes have been observed in experiments (Hart (1971)), and observed in OBLs in lakes associated with internal seiche waves (Lorke *et al.* (2005)) and internal gravity waves (Lorke *et al.* (2008)). Similar boundary layer gravitational instabilities have been observed in the flood (i.e. upslope) phase of estuarine tidal flows (Simpson *et al.* (1990), Chant & Stoner (2001), Geyer & MacCready (2014)), formed by a combination of bottom friction and the straining of horizontal buoyancy gradients over shallow finite topography.

Supercritical slope OBL laboratory experiments by Hart (1971) identified spanwise plumes and rolls (described by the streamwise, or across-slope vorticity component), associated with the periodic reversals of the density gradient, that qualitatively resembled the rolls that appeared in high Rayleigh number Couette flow experiments by Bénard & Avsec (1938), Chandra (1938), and Brunt (1951). Perhaps due to the similarity to the convection experiments, the rolls observed by Hart (1971) are often referred to as “convective rolls” although the term is misleading because it implies diabatic processes are at work; the gravitational instabilities, rolls, and overturns of interest in this study are locally adiabatic. Linear stability analyses by Deardorff (1965), Gallagher & A. Mercer (1965), and Ingersoll (1966), revealed that the observed growth of gravitationally unstable disturbances in high Rayleigh number Couette flows is suppressed in the plane of the shear (the streamwise-vertical plane) by the shear itself (i.e. the suppression of the spanwise vorticity disturbances). However, they also found that the growth of disturbances in the spanwise-vertical plane (streamwise vorticity disturbances) is unimpeded by the shear and grows in the same manner as pure convection. It has since been established that streamwise (the across-isobath direction) vortices with axes in the direction of a mean shear flow (a.k.a. “rolls”) can arise due to heating or centrifugal effects (Hu & Kelly (1997)). Therefore, since the upslope phase of the OBL is dynamically similar to gravitationally unstable Couette flow, we hypothesize that that linear streamwise vorticity disturbances may be an important mode of instability in OBLs.

In this study, we analyze the Floquet stability of the coupled streamwise vorticity component (ζ_1 , pointing in the across-isobath x direction in Figure 2) and buoyancy anomaly (aligned with $-g$ in Figure 2) in a diffusive, Boussinesq flow on an adiabatic slope when forced by an oscillating body force that represents the pressure gradient of a low-wavenumber internal wave,

$$F(t) = -A \sin t, \quad (2.2)$$

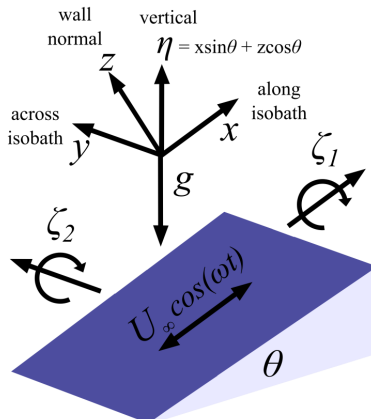


FIGURE 2. Coordinate system and vorticity components.

where A is the amplitude of the non-dimensional pressure gradient, and x is the across-slope coordinate (up/down the slope). The coordinate system, rotated angle θ counterclockwise from horizontal, and the vorticity components are shown in Figure 2.

2.1. Stationary and oscillating base flow components

The Boussinesq, dimensional form of the the conservation equations for mass and momentum are

$$\nabla \cdot \tilde{\mathbf{u}} = 0, \quad (2.3)$$

$$\partial_t \tilde{\mathbf{u}} + \tilde{\mathbf{u}} \cdot \nabla \tilde{\mathbf{u}} = -\nabla \tilde{p} + \nu \nabla^2 \tilde{\mathbf{u}} + (\tilde{b} \sin \theta + F(t)) \mathbf{i} + \tilde{b} \cos \theta \mathbf{k}, \quad (2.4)$$

$$\partial_t \tilde{b} + \tilde{\mathbf{u}} \cdot \nabla \tilde{b} = \kappa \nabla^2 \tilde{b}, \quad (2.5)$$

where θ is the counterclockwise angle of the slope from horizontal and the coordinates \mathbf{i} , \mathbf{j} , and \mathbf{k} point in the across-isobath, along-isobath, and wall-normal directions. The buoyancy is defined by density anomalies from the background flow, $\tilde{b} = g(\rho_0 - \tilde{\rho})/\rho_0$, where g is the gravitational acceleration, $\tilde{\rho}$ is the anomalous density, and ρ_0 is the reference density. The pressure \tilde{p} is defined as the mechanical pressure divided by the reference density. The buoyancy frequency is defined by the hydrostatic background $N = \sqrt{-g/\rho_0(\partial \tilde{\rho}/\partial x \sin \theta + \partial \tilde{\rho}/\partial z \cos \theta)}$ where $\tilde{\rho}(x, z) + \rho_0$ is the hydrostatic background density field. The domain is semi-infinite, bounded only by a sloped wall at $z = 0$ with no-slip, impermeable, and adiabatic boundary conditions,

$$\tilde{\mathbf{u}}(x, y, 0, t) = 0, \quad (2.6)$$

$$\partial_z \tilde{b}(x, y, 0, t) = 0. \quad (2.7)$$

At $z \rightarrow \infty$ the flow has two components: a stationary, quiescent, stably stratified, and hydrostatic component and an across-isobath, adiabatic, balanced, oscillation in the buoyancy, velocity, and pressure fields. These two components prescribe the boundary conditions at $z \rightarrow \infty$

$$\tilde{\mathbf{u}}(x, y, \infty, t) = U_\infty(t), \quad (2.8)$$

$$\partial_z \tilde{b}(x, y, \infty, t) = N^2 \cos \theta. \quad (2.9)$$

Boundary conditions for the pressure field are not required because the pressure field is diagnosed from the other variables for both flow components. Let the prognostic

variables be decomposed linearly into two components, denoted by the subscript ‘‘S’’ for the stationary component and the primed variables for the oscillating component,

$$\tilde{\mathbf{u}}(y, z, t) = \mathbf{u}_S(z) + \mathbf{u}'(y, z, t), \quad (2.10)$$

$$\tilde{b}(x, y, z, t) = b_S(x, z) + b'(y, z, t), \quad (2.11)$$

The stationary flow has no variability, other than hydrostatically balanced gradients, in the wall-tangent directions such that $\partial_x = \partial_y = 0$ and contains non-zero velocities only in the across-isobath component within a diffusion-driven boundary layer at the wall. The stationary flow is itself a linear superposition of a diffusion-driven boundary layer component and a quiescent, hydrostatic component, and the stationary flow solutions were derived by Phillips (1970) and Wunsch (1970).

Let us decompose the oscillating component into two components: a base flow component that is the hydrostatic response to the across-isobath momentum forcing (Equation 2.2), which includes a boundary layer in which friction and the diffusion of the adiabatic boundary condition break the inviscid balance of across-isobath heaving of isopycnals, and infinitesimal disturbances to the buoyancy and across-isobath vorticity,

$$\mathbf{u}'(y, z, t) = \mathbf{U}(z, t) + \epsilon \hat{\mathbf{u}}(y, z, t), \quad (2.12)$$

$$b'(y, z, t) = B(z, t) + \epsilon \hat{b}(y, z, t), \quad (2.13)$$

where $0 < \epsilon \ll 1$ and the capitalized variables represent the base flow and the hatted variables represent the infinitesimal disturbances. The base flow solutions include only an across-isobath velocity component, and zero variability in the wall-tangent directions (x and y) is also assumed for the base flow component.

The relationship between the amplitude A of the balanced oscillations and the criticality parameter reveal that the base flow is an internal wave packet that is generated at or reflected by a topographic feature when the horizontal length scales of the feature and the internal wave are much greater than the relevant boundary layer length scales. The governing equations for the balanced, inviscid oscillations that are set in motion by the momentum forcing can be derived from Equations 2.3 through 2.5 by assuming no variability in any direction for the momentum and buoyancy and by assuming that the flow is adiabatic and quiescent in the along-isobath and wall-normal directions everywhere ($V_\infty, W_\infty = 0$),

$$\partial_t U_\infty = B_\infty \sin \theta - A \sin t \quad (2.14)$$

$$\partial_t B_\infty = -U_\infty N^2 \sin \theta, \quad (2.15)$$

The solutions to the balanced, inviscid oscillations governed by Equations 2.14 and 2.15 are

$$U_\infty(t) = -U_0 \cos t, \quad (2.16)$$

$$B_\infty(t) = B_0 \sin t, \quad (2.17)$$

which requires a specific relationship between the forcing acceleration amplitude A , the forcing frequency ω , the forcing velocity amplitude U_0 , and the criticality parameter must be satisfied,

$$A = U_0 \omega (C^2 - 1). \quad (2.18)$$

Either the momentum or buoyancy amplitude U_0 or B_0 can be prescribed so long as the other satisfies

$$\frac{B_0}{U_0} = CN. \quad (2.19)$$

ϕ_1	-1
ϕ_2	-1
δ_1, δ_2	$(\frac{\omega}{4\nu}(1+Pr) \pm (\frac{\omega^2}{16\nu^2}(1+Pr)^2 + Pr(\frac{N^2 \sin^2 \theta - \omega^2}{4\nu^2}))^{1/2})^{-1/2}$
α_1	$(\omega\delta_1^2 - 2\nu Pr^{-1})/(L_b\omega\delta_1)$
α_2	0
α_3	$(2\nu Pr^{-1} - \omega\delta_2^2)/(L_b\omega\delta_2)$
α_4	0
β_1	δ_1/L_b
β_2	0
β_3	$-\delta_2/L_b$
β_4	0
L_b	$(\delta_1 - \delta_2)(2\nu Pr^{-1} + \omega\delta_1\delta_2)/(\omega\delta_1\delta_2)$

TABLE 1. Solution coefficients for subcritical slopes, $C < 1$, where $Pr = 1$. δ_1 , δ_2 , and L_b have units of length, all others are dimensionless.

Equation 2.18 indicates that the approximation of a isopycnal heaving by large horizontal wavelength internal wave on a similarly large horizontal wavelength topographic feature breaks down ($A \rightarrow 0$) as the slope angle vanishes $\theta \rightarrow 0$ or slope-parallel buoyancy oscillations resonate with the forcing $C \rightarrow 1$, a.k.a. critical slope. This is consistent with internal wave theory, which indicates that at critical slope balanced, inviscid oscillations become highly nonlinear (Dauxois & Young (1999)).

Baidulov (2010) derived solutions to for base flow,

$$U(z, t) = U_0 \text{Re} \left[\left((\alpha_1 + i\alpha_2)e^{(1+i)z\phi_1/\delta_1} + (\alpha_3 + i\alpha_4)e^{(1+i)z\phi_2/\delta_2} - 1 \right) e^{i\omega t} \right], \quad (2.20)$$

$$B(z, t) = B_0 \text{Re} \left[\left((\beta_1 + i\beta_2)e^{(1+i)z\phi_1/\delta_1} + (\beta_3 + i\beta_4)e^{(1+i)z\phi_2/\delta_2} - 1 \right) i e^{i\omega t} \right], \quad (2.21)$$

which satisfies the boundary conditions shown in Equations 2.6, 2.7, 2.8, and $\partial_z B(z \rightarrow \infty, t) = 0$. The real solutions for U and B are split into two sets of solutions corresponding to the sign of

$$\phi = \frac{\omega(1+Pr)}{\nu} - \sqrt{\frac{\omega^2(1+Pr)^2}{\nu^2} + 4\frac{Pr(N^2 \sin^2 \theta - \omega^2)}{\nu^2}}. \quad (2.22)$$

If the Prandtl number,

$$Pr = \frac{\nu}{\kappa}, \quad (2.23)$$

is unity then the expression simplifies to

$$\phi = \frac{2\omega}{\nu}(1-C), \quad (2.24)$$

thus whether the criticality parameter C is greater than or less than unity determines the base flow boundary layer dynamics. In this study $Pr = 1$, and the solution coefficients for both subcritical and supercritical flows are provided in Tables 1 and 2. If $C = 1$ the base flow is an oscillation at the natural frequency of the system.

2.2. Ratio of stationary and oscillating time scales

Across-isobath vorticity disturbances can grow from the stationary flow component and/or the oscillating base flow component. In this study, Floquet analyses are only applied to examine the linear growth of disturbances to the oscillating base flow alone

ϕ_1	-1
ϕ_2	i
δ_1, δ_2	$\left(\left(\frac{\omega^2}{16\nu^2} (1 + Pr)^2 + Pr \left(\frac{N^2 \sin^2 \theta - \omega^2}{4\nu^2} \right) \right)^{1/2} \pm \frac{\omega}{4\nu} (1 + Pr) \right)^{-1/2}$
α_1	$\left(\frac{\delta_1}{\omega L_b^4} - \frac{2\kappa}{\delta_1 \omega^2 L_b^4} \right) (\omega \delta_1^2 \delta_2 - 2\kappa \delta_2)$
α_2	$\left(\frac{\delta_1}{\omega L_b^4} - \frac{2\kappa}{\delta_1 \omega^2 L_b^4} \right) (2\kappa \delta_1 + \omega \delta_1 \delta_2^2)$
α_3	$\left(\frac{2\kappa}{\delta_2 \omega^2 L_b^4} + \frac{\delta_2}{\omega L_b^4} \right) (2\kappa \delta_1 + \omega \delta_1 \delta_2^2)$
α_4	$\left(\frac{2\kappa}{\delta_2 \omega^2 L_b^4} + \frac{\delta_2}{\omega L_b^4} \right) (2\kappa \delta_2 - \omega \delta_1^2 \delta_2)$
β_1	$\frac{\delta_2}{\omega L_b^4} (\omega \delta_1 \delta_2^2 + 2\kappa \delta_1)$
β_2	$\frac{\delta_2}{\omega L_b^4} (2\kappa \delta_2 - \omega \delta_1^2 \delta_2)$
β_3	$\frac{\delta_1}{\omega L_b^4} (\omega \delta_1^2 \delta_2 - 2\kappa \delta_2)$
β_4	$\frac{\delta_1}{\omega L_b^4} (\omega \delta_1 \delta_2^2 + 2\kappa \delta_1)$
L_b	$\left(\frac{(\delta_1^2 + \delta_2^2)(\omega^2 \delta_1^2 \delta_2^2 + 4Pr^{-2}\nu^2)}{\omega^2 \delta_1 \delta_2} \right)^{1/4}$

TABLE 2. Solution coefficients for supercritical slopes, $C > 1$, where $Pr = 1$. δ_1 , δ_2 , and L_b have units of length, all others are dimensionless.

because the disturbances are much more rapidly modulated by the oscillating flow component than the stationary flow component; thus, the stationary flow can be neglected.

A ratio of flow time scales illustrates why, for the parameter ranges applicable to the abyssal ocean, the stationary flow can be neglect from Floquet analyses of the disturbances. The wall normal diffusive time scale is the relevant characteristic time scale of the stationary diffusion-driven flow because the diffusion of the adiabatic boundary condition into the interior induces the boundary layer baroclinic vorticity and momentum (Dell & Pratt (2015)). Following Dell & Pratt (2015), the time scale of the non-rotating flow is

$$\tau_\kappa \sim \delta_0^2 / \kappa, \quad (2.25)$$

$$\sim \frac{\sqrt{Pr}}{N \sin \theta}, \quad (2.26)$$

where the boundary layer thickness of the non-rotating stationary diffusion-driven boundary layer is

$$\delta_0 = \left(Pr \frac{N^2 \sin^2 \theta}{4\nu^2} \right)^{-1/4}. \quad (2.27)$$

Therefore, the modulation ratio (Davis (1976)) is

$$\mathcal{T} \sim \frac{\tau_\kappa}{\tau_\omega} = \frac{\omega \delta_0^2}{\kappa}. \quad (2.28)$$

In the limit of $\mathcal{T} \rightarrow \infty$, the time scale separation between the stationary diffusion-driven flow component and the oscillating flow component indicates that the slower stationary diffusion-driven flow component does not modulate the faster oscillatory flow component. If $\mathcal{T} \rightarrow 0$, the oscillating flow component varies so slowly relative to the stationary diffusion-driven flow component that the steady flow component may alter the instabilities of the oscillating component.

The modulation ratios (Equation 2.28) for typical abyssal parameter ranges for the M_2 tide are shown in Figure 3, which indicates that as $\theta \rightarrow 0$, the stationary diffusion-

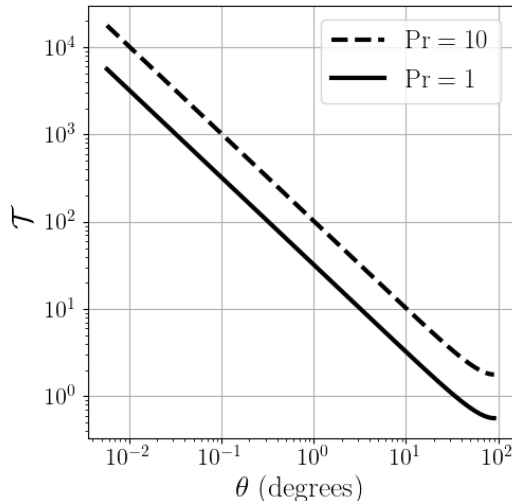


FIGURE 3. Modulation ratios.

driven flow component does not modify the much faster dynamics of the oscillatory flow component. The time scale separation of at least $\mathcal{O}(10^2)$, valid for approximately $0 < \theta < 1^\circ$ (0.0175 rad), a range of slopes commonly found in deep ocean bathymetry (Goff & Arbic (2010)), informs our neglect of the stationary diffusion-driven flow component and application of Floquet analysis to the oscillatory flow component alone. While we consider the case of $Pr = 1$, note that the time scale separation increases for $Pr = 10$.

2.3. Governing equations for spanwise disturbances

The non-dimensional parameters of the linearized governing equations for the across-isobath vorticity component and buoyancy disturbances are chosen in the same manner as was used Blennerhassett & Bassom (2002) to investigate the linear stability of Stokes' second problem, with the exceptions that we include the Boussinesq buoyancy and we analyse the across-isobath (streamwise) vorticity instead of the spanwise vorticity. The oscillating flow variables are non-dimensionalized as follows:

$$\mathbf{x} = \frac{\mathbf{x}_d}{\delta}, \quad \mathbf{u}' = \frac{\mathbf{u}'_d}{U_0}, \quad t = \omega t_d, \quad p' = \frac{p'_d}{U_0^2}, \quad b' = \frac{\omega b'_d}{N^2 U_0 \sin \theta}, \quad (2.29)$$

where subscript d denotes dimensional variables and from here forward the variables without this subscript are dimensionless. p' is the mechanical pressure divided by the reference density ρ_0 , and the buoyancy is $b' = g(\rho_0 - \rho')/\rho_0$. Note that the Eulerian time scale is not proportional to the advective time scale (i.e. $U_0/\delta \neq \omega$). The two-dimensional flow governing equations for mass, momentum, and thermodynamic energy (buoyancy) for the disturbances in the $y - z$ plane are

$$0 = \partial_y \hat{v} + \partial_z \hat{w}, \quad (2.30)$$

$$\partial_t \hat{v} = -\frac{Re}{2} \partial_y \hat{p} + \frac{1}{2} (\partial_{yy} + \partial_{zz}) \hat{v}, \quad (2.31)$$

$$\partial_t \hat{w} = -\frac{Re}{2} \partial_z \hat{p} + \frac{1}{2} (\partial_{yy} + \partial_{zz}) \hat{w} + C^2 \hat{b} \cot \theta, \quad (2.32)$$

$$\partial_t \hat{b} = -\left(\frac{Re \partial_z B(z, t)}{2} \right) \hat{w} + \frac{1}{2Pr} (\partial_{yy} + \partial_{zz}) \hat{b}, \quad (2.33)$$

where the Reynolds number and Stokes' layer thickness are

$$Re = \frac{U_0 \delta}{\nu}, \quad (2.34)$$

$$\delta = \sqrt{\frac{2\nu}{\omega}}. \quad (2.35)$$

For all analyses in this study $Pr = 1$. The streamwise vorticity component (see Figure 2) is defined:

$$\hat{\zeta}_1 = \partial_y \hat{w} - \partial_z \hat{v}. \quad (2.36)$$

Let the infinitesimal disturbances take the form of a normal mode decomposition in the spanwise (y) direction:

$$\hat{\zeta}_1(y, z, t) = \zeta_1(z, t)e^{ily} + \text{complex conjugate}, \quad (2.37)$$

$$\hat{b}(y, z, t) = b(z, t)e^{ily} + \text{complex conjugate}, \quad (2.38)$$

where the modal streamfunction ψ and modal velocities are defined

$$\zeta_1 = (\partial_{zz} - l^2)\psi, \quad (2.39)$$

$$(v, w) = (-\partial_z \psi, il\psi), \quad (2.40)$$

$$l = l_d \delta = \frac{2\pi}{\lambda} \delta \quad (2.41)$$

Finally the governing equation for the evolution of the streamwise vorticity modes is

$$\partial_t \zeta_1 = \underbrace{\frac{(\partial_{zz} - l^2)}{2} \zeta_1}_{\text{diffusion}} + \underbrace{ilC^2 b \cot \theta}_{\text{baroclinic production of vorticity}}, \quad (2.42)$$

and the governing equation for the evolution of the associated buoyancy is

$$\partial_t b = \underbrace{\frac{(\partial_{zz} - l^2)}{2Pr} b}_{\text{diffusion}} - \underbrace{\frac{\partial_z B(z, t) ilRe}{2} \psi}_{\text{advection of base buoyancy}}. \quad (2.43)$$

There are no terms representing the advection of disturbances by the base flow in Equations 2.42 and 2.43, nor the advection of base vorticity by vorticity disturbances. The basic state flow enters the equations only through the advection of base buoyancy by the buoyancy disturbances (the first term on the right hand side of Equation 2.33); therefore, disturbance vorticity can only be produced by gravitational instabilities. The state vector for Equations 2.42 and 2.43 is

$$\mathbf{x}(z, t) = \begin{bmatrix} \zeta_1(z, t) \\ b(z, t) \end{bmatrix}, \quad (2.44)$$

and the dynamical operator for the evolution of the principal fundamental solution matrix (Equation A 8) is

$$\mathbf{A}(z, t) = \begin{bmatrix} \frac{(\partial_{zz} - l^2)}{2} & ilC^2 \cot \theta \\ -\frac{\partial_z B(z, t) ilRe (\partial_{zz} - l^2)^{-1}}{2} & \frac{(\partial_{zz} - l^2)}{2Pr} \end{bmatrix}. \quad (2.45)$$

2.4. Discrete Floquet exponents, modes, and multipliers

Let the disturbance state vector \mathbf{x} be composed of two variables that vary in a single dimension (z), vorticity ζ and Boussinesq buoyancy b , that are discretized onto a grid of

N_z discrete points in the z coordinate takes the form

$$\mathbf{x}(t) = \begin{bmatrix} \zeta(z_1, t) \\ \vdots \\ \zeta(z_{N_z}, t) \\ b(z_1, t) \\ \vdots \\ b(z_{N_z}, t) \end{bmatrix} = \begin{bmatrix} x_1(t) \\ \vdots \\ x_M(t) \end{bmatrix}, \quad (2.46)$$

where the length of state vector \mathbf{x} is $M = N_v \times N_z$ (the number of variables multiplied by the number of grid points). The principal fundamental solution matrix $\Phi_p(t)$ for state vector $\mathbf{x}(t)$ is defined as

$$\Phi_p(t) = \begin{bmatrix} x_{1,1}(t) & \dots & x_{1,M}(t) \\ \vdots & \ddots & \vdots \\ x_{M,1}(t) & \dots & x_{M,M}(t) \end{bmatrix}. \quad (2.47)$$

The principal fundamental solution matrix at time $t = T$ (T being the oscillation period) can be analyzed to determine the fastest growing Floquet mode and discrete grid location of the largest Floquet multiplier (see Appendix A for the derivation and formal properties of the principal fundamental solution matrix). At time $t = 0$ the principal fundamental solution matrix is an identity matrix that can be physically interpreted as a set of independent linear perturbations of the system; thus, each Floquet mode represents an initial disturbance at each discrete grid location.

The innovation of Floquet (1883) was the recognition that, without a loss of generality, the initial conditions specified at time $t = t_0$ can be expressed in terms of the eigenvectors of the principal fundamental solution matrix after one oscillation period has elapsed, $t = t_0 + T$. Choosing $t_0 = 0$,

$$\Phi_p(T)\mathbf{v}(0) = \boldsymbol{\mu}\mathbf{I}\mathbf{v}(0) \quad (2.48)$$

where $\boldsymbol{\mu}$ is a vector of the eigenvalues of $\Phi_p(T)$ and \mathbf{v} are the eigenvectors of $\Phi_p(T)$ such that $\mathbf{v}(0) = \mathbf{x}(0)$ and therefore $\mathbf{v}(T) = \mathbf{x}(T)$. $\mathbf{v}(t)$ are the Floquet modes and $\boldsymbol{\mu}$ are the Floquet multipliers. Therefore,

$$\mathbf{v}(T) = \boldsymbol{\mu}\mathbf{I}\mathbf{v}(0), \quad (2.49)$$

is equivalent to Equation A 7. The stability of the system in terms of Floquet multipliers is:

- (a) If *all* Floquet multipliers (i.e. eigenvalues) satisfy $\text{Re}[\mu] < 1$, then all disturbances decay as $t \rightarrow \infty$ and the system is **stable**.
- (b) If *any* Floquet multipliers satisfy $\text{Re}[\mu] = 1$ and the rest satisfy $\text{Re}[\mu] < 1$, then then the stability of the system is **periodic** as $t \rightarrow \infty$. Periodic modes do not necessarily oscillate at the base frequency, only if $\mu \pm 1 + 0i$ then the mode's frequency exactly matches the base flow.
- (c) If *any* Floquet multiplier satisfies $\text{Re}[\mu] > 1$, then the disturbance will grow in amplitude as $t \rightarrow \infty$ and the system is **unstable**.

Floquet multipliers are generally complex. For fluid flows, however, the component of interest is the real part of μ . The Floquet solutions are the columns of the principal fundamental solution matrix while the Floquet modes are defined by the Floquet exponents

$$\gamma = \frac{\log \boldsymbol{\mu}}{T}, \quad (2.50)$$

where exponents are complex. The Floquet modes are defined

$$\mathbf{v}(t) = \exp(\text{Re}[\gamma]t)\mathbf{P}(t)\mathbf{v}(0), \quad (2.51)$$

thus

$$\text{Re}[\Phi_p(T)] = \exp(\text{Re}[\gamma]T), \quad (2.52)$$

where $\mathbf{P}(t)$ are periodic Floquet mode components (harmonics of the base frequency) and the Floquet multipliers can be expressed as $\boldsymbol{\mu} = \exp(\text{Re}[\gamma]T)$ because $\mathbf{P}(T) = \exp(\text{Im}[\gamma]T) = 1$. The real part of the Floquet exponents corresponds to the growth or decay of the mode as $t \rightarrow \infty$ and the imaginary part of the Floquet exponent determines the frequency of the Floquet mode in terms of harmonics of the base frequency. Further Floquet theory details are provided in Appendix A.

2.5. Boundary conditions

The oscillatory forcing was imposed by imposing a ‘‘moving wall’’ boundary condition rather than applying a body force directly on the evolving modes. At the moving wall, the total flow boundary conditions on the momentum are no-slip and impermeable; therefore, at $z = 0$

$$\mathbf{u}' = U\mathbf{i} + \epsilon\hat{\mathbf{u}} = \cos t\mathbf{i}, \quad (2.53)$$

where $0 < \epsilon \ll 1$ is a small parameter and

$$U(0, t) = \cos t, \quad (2.54)$$

therefore

$$\partial_z \psi = 0, \quad (2.55)$$

is required to satisfy the no-slip condition at $z = 0$ for either definition of the streamfunction. The streamfunction must be constant along an impermeable wall; therefore it is numerically convenient to choose

$$\psi = 0, \quad (2.56)$$

at $z = 0$ to satisfy $w = \partial_x \psi = 0$ for the spanwise vorticity - streamfunction approach or $w = \partial_y \psi = 0$ for the streamwise vorticity - streamfunction approach.

The wall is adiabatic; therefore,

$$\partial_z b' = \partial_z B + \epsilon \partial_z \hat{b} = 0. \quad (2.57)$$

Since the basic state stratification satisfies

$$\partial_z B = 0, \quad (2.58)$$

then the disturbance stratification must satisfy

$$\partial_z \hat{b} = 0, \quad (2.59)$$

at $z = 0$.

At $z \rightarrow \infty$, the conventional boundary conditions for Stokes’ second problem are parallel and irrotational flow. Parallel flow is ensured if

$$\psi = 0, \quad (2.60)$$

at $z \rightarrow \infty$. Irrotational flow at $z \rightarrow \infty$ is prescribed by

$$\zeta_1 = 0. \quad (2.61)$$

The background stratification is not adiabatic in the far field. but the disturbance

stratification can be adiabatic because the basic flow gradients exist only in the boundary layer. Therefore, at $z \rightarrow \infty$

$$\partial_z b = 0. \quad (2.62)$$

3. Numerical methods

As described in section 2.4, the length of the perturbation state vector \mathbf{x} is $N_v \times N_z$, where N_v is the number of variables and N_z is the number of grid points. In the streamfunction-vorticity formulation in this study $N_v = 2$ for vorticity and buoyancy. The number of grid points in z , the wall-normal direction, for all calculations was $N_z = 200$. Therefore the discrete principal fundamental solution matrix is a square matrix with $2N_z$ rows and columns. The variables were computed at the cell centers of a uniform grid of height $H/\delta = 32$, where the non-dimensional grid encompassed $z = [0, H/\delta]$. Previous studies found that Floquet stability calculations for Stokes' second problem were unaffected by an upper domain boundary as long as it was located at $H/\delta = 32$ or greater (Blennerhassett & Bassom (2006), Luo & Wu (2010)).

Centered second-order finite difference schemes were used to compute the discrete forms of all first and second derivatives and the vorticity inversions that appear the dynamical operator $\mathbf{A}(z, t)$ for (Equation 2.45). To implement the no-slip, impermeable boundary conditions at the wall (Equations 2.55, 2.56), the streamfunction and its z derivative were set to zero. However, to guarantee unique solutions at second-order accuracy, the vorticity at the wall was required to compute the second derivatives of the vorticity. The second-order accuracy was confirmed with grid convergence tests shown in Appendix B. A second-order accurate extrapolation of the vorticity at the wall that accounts for no-slip and impermeable boundary conditions was derived by (Woods (1954)) for this purpose. The Woods (1954) boundary condition is:

$$\zeta(0, t) = \frac{3}{\Delta z^2} \psi(z_1, t) - \frac{1}{2} \zeta(z_1, t), \quad (3.1)$$

where $z = 0$ denotes variables located at the wall and $z = z_1$ denotes variables located at the first cell center. All of the other boundary conditions (Equations 2.59, 2.60, 2.61, and 2.62) were readily implemented into the discrete derivatives within the discrete form of the operator $\mathbf{A}(z, t)$. Finally, test functions were used to ensure that the truncation error for all discrete derivative and inversions decreased with $(\Delta z)^{-2}$, where Δz is the height of a grid cell.

To obtain the principal fundamental solution matrix at time $t = T$, Equation A 8 was integrated over one period with the standard explicit fourth order Runge-Kutta time advancement method, equivalent to simultaneously solving the evolution of the state vector in Equation A 1 in which each linearly independent solution begins with each linearly independent initial condition as defined in Equation A 6. The method for computing the principal fundamental solution matrix in this study is formally second-order accurate.

3.1. Solver verification

The neutral stability curve for Stokes' second problem was computed as a code verification test, shown in Figure 4. There the blue line is the computed neutral stability curve, and the pink line is a least squares fit of the computed neutral stability curve. The yellow line is a least squares fit of the computed stability curve by Blennerhassett & Bassom (2002), who used a spectral method for the computation, and the blue dots were calculated by linearized direct numerical simulations by Luo & Wu (2010). The

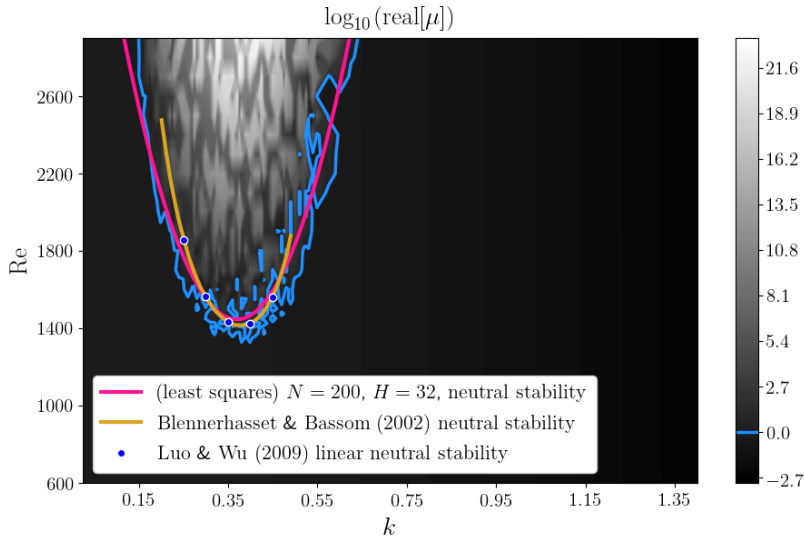


FIGURE 4. The neutral stability curve for Stokes' second problem.

Verification of spatial discretization, temporal discretization, and eigenvalue calculation. The computed Floquet multipliers are shown by the gray shading, and the calculated $\text{Re}[\mu] = 1$ contour is represented with the blue line.

variations in the neutral stability curve about the pink line can be attributed to the spatial discretization method. This hypothesis is supported by the Floquet results for the neutral stability curve for Mathieu's equation (see Appendix B), which has no spatial derivatives and was computed to graphical accuracy using the same code for time integration and eigenvalue calculation.

The irregularities of the blue neutral stability curve in Figure 4 occur because of the initialization of the principal fundamental solution matrix as an identity matrix. In the first time step of the calculation, the finite differencing of discontinuous functions (specifically Dirac delta functions) introduces discretization errors that do not converge with increased grid resolution. To check this, the stability of Stokes' second problem was computed for varied Reynolds number and grid resolution at $k = 0.35$, as shown in Figure 5. The Floquet multipliers in Figure 5 that correspond to stable points in the neutral stability plot of Figure 4 converge quickly with increasing grid resolution. However, for $Re \geq 1400$, $k = 0.35$ (inside the unstable region of Figure 4) the multipliers in Figure 5 do not converge with increasing grid resolution. Luo & Wu (2010) pointed out that SSP stability calculations are extremely sensitive to transient noise that occurs during the course of the oscillation, which suggests that small round-off errors and other numerical noise may explain the variations of the stability curve fit calculated by Blennerhasset & Bassom (2002). Figure 5 indicates that the primary culprit for transient noise in the present study is the introduction of discretization errors at the first time step. Therefore the $N_z = 200$ was deemed sufficient grid resolution, and the calculated neutral stability curves from a finite difference method must be considered approximate rather than exact.

4. Results

Figure 6 depicts the results of Floquet analysis of vorticity and buoyancy disturbances governed by Equations 2.42 and 2.43, respectively, which indicate that the system is

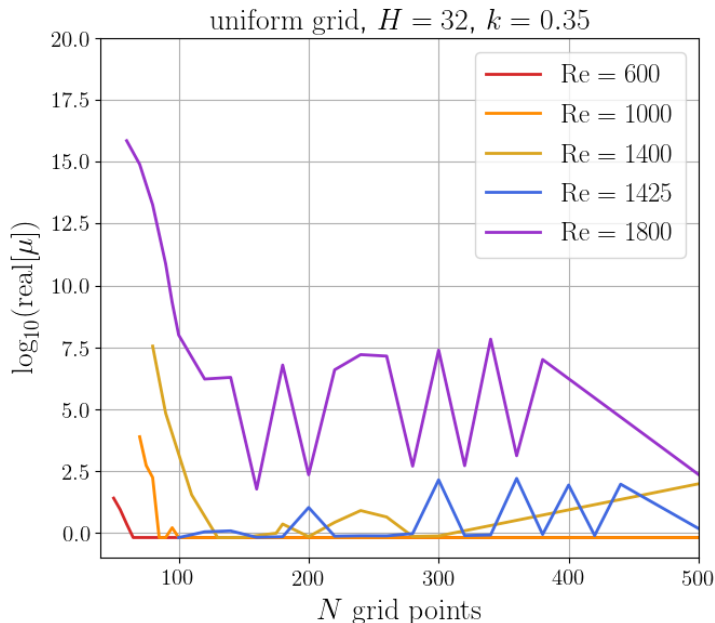


FIGURE 5. Grid convergence occurs only for stable calculations.

Stable Floquet multiplier calculations achieve grid convergence. Near the neutral stability curve, the Floquet multiplier calculations fail to achieve grid convergence

because finite differences of the identity matrix initial condition of the principal fundamental solution matrix introduce grid independent noise. Therefore the “wiggles” of the blue curve in Figure 4 are due to the sensitivity of the multiplier value to noise introduced at just after $t = 0$ when finite differences are taken of discontinuities in the principal fundamental solution matrix.

increasingly linearly unstable as the Reynolds number, criticality parameter, and non-dimensional spanwise disturbance wavenumber are increased. $Re < 10$ and $l < 0.5$, approximately, are maximum Reynolds number and disturbance wavelength required for stability for the entire investigated parameter space. At $C \ll 1$ the minimum Reynolds number necessary for global linear instability increases, and the forcing of vorticity disturbances by buoyancy disturbances decreases because baroclinic production term on the right hand side of Equation 2.42 vanishes in the limit $C \rightarrow 0$. Therefore, increased stability at small $C \ll 1$ suggests that baroclinic production of disturbance vorticity is the primary mechanism of instability. This result is in agreement with the empirical and approximate stability criteria of Hart (1971) which posits that the flow is globally stable if $C^2 \ll 1$.

If ω , N , and θ constant, Equation 2.19 indicates that increasing the oscillation velocity amplitude U_0 and thus the Reynolds number will increase the amplitude of the buoyancy oscillations B_0 as well. Since the boundary layer thicknessness δ_1, δ_2 do not depend on U_0 and they determine the length scale of the boundary layer buoyancy gradient, the boundary layer buoyancy gradient increases with increasing Reynolds number and both quantities force buoyancy disturbances through the second term on the right hand side of Equation 2.43.

The system is stable to large spanwise wavelength disturbances because all of the terms on the right hand sides of the disturbance Equations 2.42 and 2.43 vanish except for the

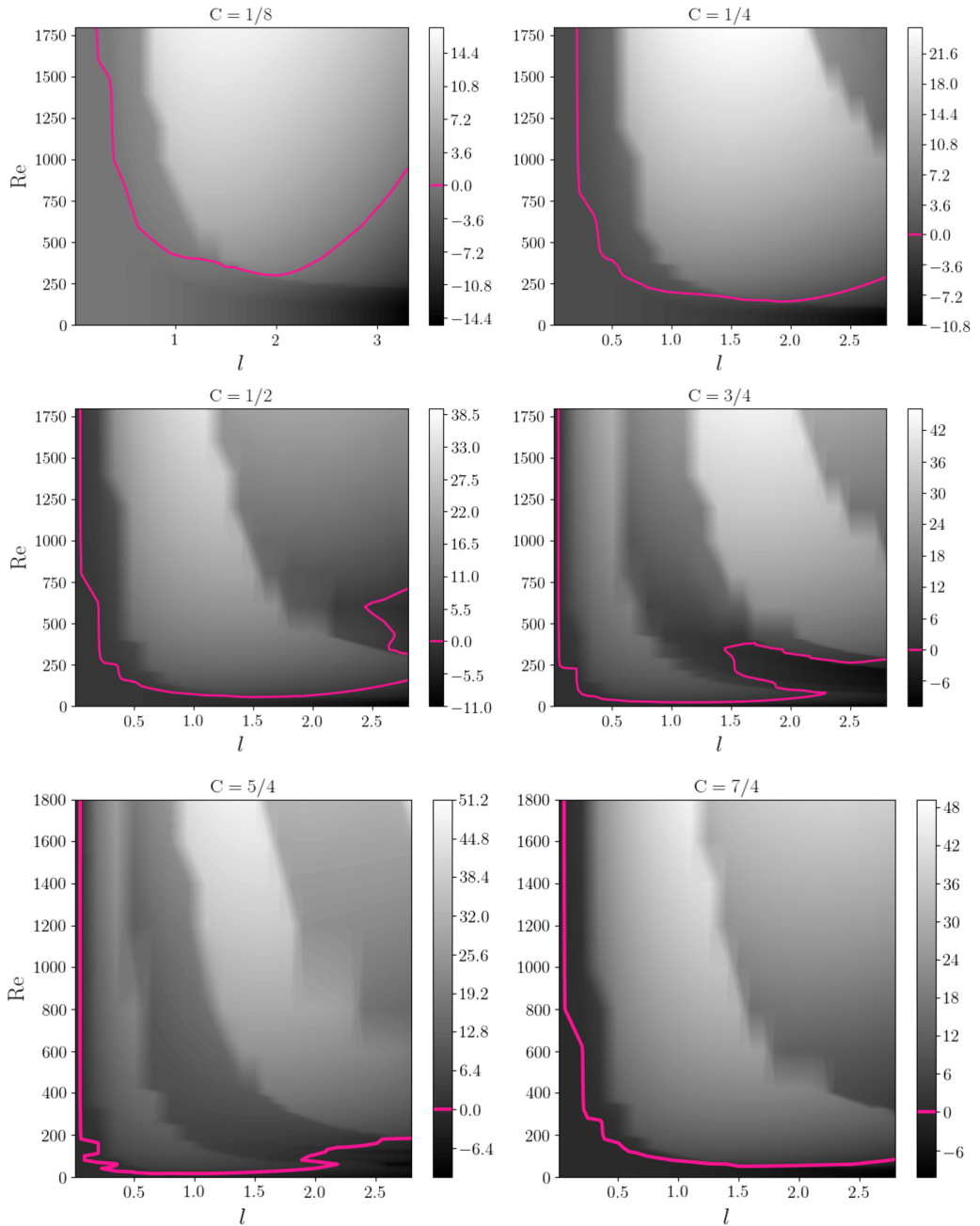
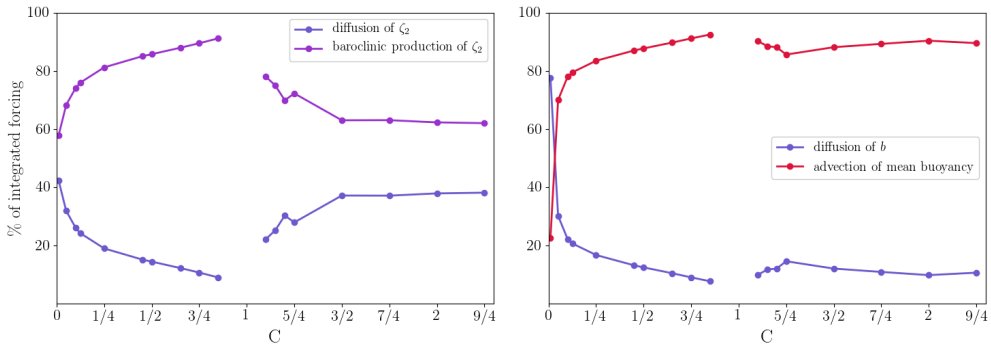


FIGURE 6. $\log_{10}(\text{Re}[\mu])$ for the streamwise vorticity, ζ_1 , for subcritical and supercritical slopes as functions of criticality parameter ($C = N \sin \theta / \omega$), Reynolds number ($Re = U_0 \delta / \nu$), and spanwise disturbance wavenumber ($l = 2\pi \delta / \lambda$). The pink lines are the Floquet neutral stability curves ($\text{Re}[\mu] = 1$, $\text{Re}[\gamma] = 0$).


 FIGURE 7. Integrated ζ_1 , b , budgets for $Re = 420, l = 1.0$.

Percentages of the right hand sides of Equations 2.42 and 2.43 calculated by spatio-temporal integration of $\mathbf{A}(z, t)$, for the most unstable Floquet mode at each value of C . The flow is Floquet unstable at $Re = 420, l = 1.0$ for all C investigated, therefore the dominant mechanisms induce disturbance growth.

diffusion of disturbances in the wall normal direction in the limit as $l \rightarrow 0$. Growing disturbances described by Equation 2.45 are confined to the boundary layer because they are forced by the base flow buoyancy gradient that vanishes outside the boundary layer; disturbances that propagate outside of the boundary layer are diffused.

The fingers on the low Reynolds number, higher l portions of the neutral stability curves shown in Figure 6 at $C = 1/2$ and $C = 3/4$ merit further examination. However, irregularities in neutral stability curves have also been found in the neutral stability curve for Stokes' second problem (Blennerhassett & Bassom (2002)).

Each equation term in matrix $\mathbf{A}(z, t)$ (Equation 2.45) was integrated in z and t for the fastest growing Floquet mode (the mode with maximum μ , where $\mu > 1$) to qualitatively assess the dominant physical mechanisms of the fastest growing linear disturbances. The terms were normalized by the total right hand side forcing, corresponding to the rows of $\mathbf{A}(z, t)$, such that the temporally and spatially integrated forcings sum to unity. The integrated equation term results are shown in Figure 7 suggests that, on both subcritical and supercritical slopes, the fastest growing linearly unstable disturbances are amplified by the non-diffusive terms in Equations 2.42 and 2.43, and that the diffusive terms increasingly inhibit the growth of linear instabilities at $C \ll 1$.

The inherent three dimensionality of the gravitational instability initiated by spanwise buoyancy disturbances (Equation 2.38) to the streamwise vorticity component is evident in the total baroclinic vorticity production term that can be derived from by linearizing and taking the curl of the momentum equation (Equation 2.4),

$$\text{total baroclinic vorticity production} = C^2 (ilb(z, t)e^{ily} \cot \theta \mathbf{i} - \partial_z B \mathbf{j} - ilb(z, t)e^{ily} \mathbf{k}). \quad (4.1)$$

Equation 4.1 reveals that spanwise buoyancy disturbances force the streamwise and wall-normal vorticity components. This suggests that the growth of linear gravitational instabilities induced by spanwise disturbances must induce three dimensional motion, a phenomena that is widely observed in other stratified shear flow instabilities (Peltier & Caulfield (2003)), and it suggests that the full three-dimensional dynamics must be considered to accurately assess the growth of linear instability as $t \rightarrow \infty$. Comparison of the Floquet analysis results with the downslope relaminarization of initially two-dimensional spanwise rolls that evolve into three-dimensional motion observed in experiments (Hart (1971)) suggests that the Floquet analysis of spanwise disturbances may be descriptive of the initial linear gravitational instability that triggers spanwise rolls,

but fails to account for the three-dimensional diffusive damping. The Floquet analysis identifies linear gravitational instabilities that exhibit net growth over the period of the oscillation despite the transience of the unstable buoyancy gradient. However, since Equation 4.1 indicates that the instabilities must become three dimensional, the growth of these linear instabilities could be suppressed or increased by three-dimensional motion. Direct numerical simulations by Kaiser (2020) suggest that low Reynolds number the growth of linear instabilities is dissipated by three-dimensional motion.

5. Conclusions

Floquet linear stability theory was applied to laminar, oscillating, stratified, viscous diffusive boundary layers on infinite slopes in non-rotating reference frames. The linear stability of a two-dimensional disturbances in the $y-z$ plane (described by the streamwise vorticity ζ_1) was evaluated within the non-dimensional parameter ranges of $0 < Re \leq 1750$, $1/8 \leq C \leq 7/4$, $0 < l \leq 3$, and $Pr = 1$. The parameter regime is consistent with idealized M_2 tidal heaving of isopycnals up and down smooth, mid-latitude abyssal slopes where $N/\omega \sim 7.1$, $0 < \theta \leq \pi/12$, $\nu \sim 2.0 \cdot 10^{-6} \text{ m}^2\text{s}^{-1}$, $\omega \sim 1.4 \cdot 10^{-4} \text{ rad s}^{-1}$, $35.4 \leq \lambda < \infty \text{ cm}$, and $0.0 < U_\infty \leq 2.1 \text{ cm s}^{-1}$.

The most salient results the Floquet analyses are

- we have shown that oscillating laminar boundary layers on adiabatic abyssal slopes are increasingly linearly unstable as Reynolds number, criticality parameter, and/or spanwise disturbance wavelength are increased;
- the mechanism of the instability is the same as for gravitationally unstable Couette flow;
- our results qualitatively agree with experiments of related flows;
- the growth of unstable Floquet modes must generate three-dimensional motions that are unaccounted for in the Floquet analyses which could suppress or increase instabilities as $t \rightarrow \infty$;
- our finite difference numerical approach is more sensitive to numerical noise in the parameter space near the neutral stability curve than spectral methods.

The linear disturbances must create three-dimensional baroclinic vorticity production. Therefore the growth of disturbances predicted by two-dimensional Floquet analysis as $t \rightarrow \infty$ may not be descriptive of the the three-dimensional flow as $t \rightarrow \infty$. However, the gravitational instability described by two-dimensional Floquet analysis is consistent with two-dimensional rolls in the $y-z$ plane observed in experiments (Hart (1971)), which suggests that the Floquet analysis results describe the initial vorticity and buoyancy mechanisms of linear gravitational instabilities on Boussinesq adiabatic slopes but not the behavior of disturbances as $t \rightarrow \infty$.

Our results validate the hypothesis that Floquet stability calculations, regardless of the chosen numerical method, are extremely sensitive to transient numerical noise that occurs throughout the oscillation period, in agreement with the conclusions of Luo & Wu (2010) for Stokes' second problem calculations. The sensitivity to the numerical errors and noise may explain the highly irregular shapes of neutral stability curves that vary from one study to the next (Blennerhassett & Bassom (2002), Luo & Wu (2010)). While the transient noise can represent actual physics that perturb disturbances randomly throughout the phase of the oscillation, the statistical characteristics of the numerical noise are not readily discernable; therefore, the disturbance conditions of the numerical calculations are impossible to exactly replicate in laboratory experiments (Luo & Wu (2010)). It was shown that the transient noise cannot be eliminated by increasing the numerical accuracy; therefore, the results of this study support the conclusion that

numerical Floquet stability calculations must be considered approximate, rather than exact, estimates of linear disturbance behavior.

6. Acknowledgements

B.K. was supported by a N.S.F. Graduate Research Fellowship and the Massachusetts Institute of Technology - Woods Hole Oceanographic Institution Joint Program, and by the National Science Foundation (OCE-1657870). The authors thank the Massachusetts Green Computing Center, Jörn Callies, Jesse Canfield, Raffaele Ferrari, Karl Helfrich, and Andreas Thurnherr. This document is approved for Los Alamos Unlimited Release, LA-UR-21-28221.

Appendix A. Floquet theory applied to tensors

In this section Floquet theory for tensors is briefly summarized to show how Floquet multipliers can be calculated directly for base flow solutions across spatial grids. The reader is referred to Iooss & Joseph (2012) for the complete derivation.

In Floquet theory for vectors or tensors, the principal fundamental solution matrix is a mapping of the state vector \mathbf{x} at time $t = 0$ to one period, $t = T$. Consider the non-autonomous system,

$$\frac{d\mathbf{x}}{dt} = \mathbf{A}(t)\mathbf{x}(t), \quad (\text{A } 1)$$

where $\mathbf{x}(t)$ is a vector and the operator $\mathbf{A}(t)$ is periodic

$$\mathbf{A}(t + T) = \mathbf{A}(t). \quad (\text{A } 2)$$

For a state vector $\mathbf{x}(t)$ of shape $[M \times 1]$, where M is the number of variables times the number of grid points, there exists a fundamental solution matrix $\Phi(t)$ of shape $[M \times M]$ and coefficient vector \mathbf{c} of shape $[M \times 1]$, such that

$$\mathbf{x}(t) = \Phi(t)\mathbf{c}. \quad (\text{A } 3)$$

The fundamental solution matrix is a non-unique matrix in which the columns are the structure of the linearly independent solutions. The magnitude of the elements in Φ depend on the choice of \mathbf{c} , and the only restriction to the choice of a tenable \mathbf{c} is that Φ be invertible. In that case, at time $t = 0$,

$$\mathbf{c} = \Phi(0)^{-1}\mathbf{x}(0) \quad (\text{A } 4)$$

Substitution of Equation A 4 into Equation A 3 yields

$$\mathbf{x}(t) = \Phi(t)\Phi(0)^{-1}\mathbf{x}(0). \quad (\text{A } 5)$$

The principal fundamental solution matrix Φ_p is just a fundamental solution matrix chosen such that at $t = 0$ it is an identity matrix:

$$\Phi_p(0) = \mathbf{I}. \quad (\text{A } 6)$$

Substitution of Equation A 6 in Equation A 5 yields

$$\mathbf{x}(T) = \Phi_p(T)\mathbf{x}(0); \quad (\text{A } 7)$$

therefore, the principal fundamental solution matrix at time $t = T$ maps the initial state $\mathbf{x}(0)$ to the final state after one period, $\mathbf{x}(T)$. By definition, Equation A 1 can be written

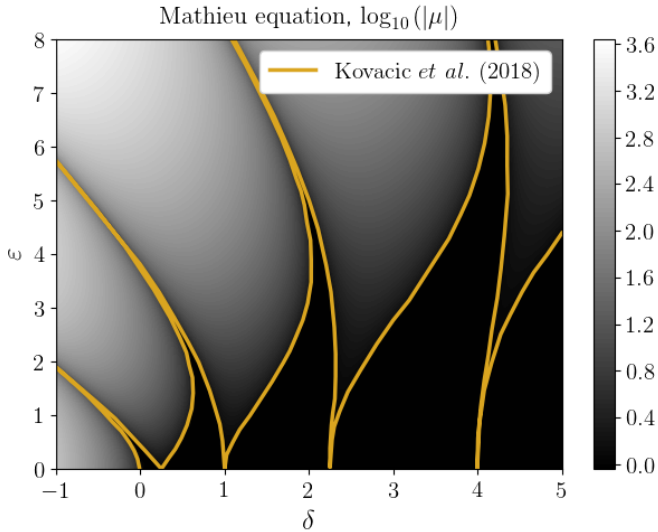


FIGURE 8. The neutral stability curve for Mathieu’s equation. Verification of the temporal discretization scheme and the eigenvalue calculation. The computed Floquet multipliers are shown by the gray shading, and the $\text{Re}[\mu] = 1$ contour lies under the yellow line of Kovacic *et al.* (2018) to graphical accuracy.

in terms of the principal fundamental solution matrix,

$$\frac{d\Phi_p}{dt} = \mathbf{A}(t)\Phi_p(t), \quad (\text{A } 8)$$

and so $\Phi_p(T)$ can be obtained directly by integrating Equation A 8 forward in time one period. The direct application of Floquet theory to a state vector describing a fluid flow has been used by Noack & Eckelmann (1994), Robichaux *et al.* (1999), and Barkley & Henderson (1996) to study instabilities in the periodic von Kármán vortex streets that develop in the wakes of cylinders.

Appendix B. Floquet analysis of Mathieu’s equation

The Mathieu equation is an ordinary differential equation of the form

$$\partial_{tt}y + f(t)y = 0, \quad (\text{B } 1)$$

where

$$f(t) = \delta + \varepsilon \cos(t). \quad (\text{B } 2)$$

The neutral stability curve of Mathieu’s equation was computed to verify the temporal discretization and is shown in Figure 8.

Appendix C. Finite difference grid convergence

Second order accurate finite difference stencils were used to form discrete matrices for the calculation of the first and second derivatives of the buoyancy disturbances (Equation 2.43), for the calculation of the second derivatives of the vorticity disturbances (Equation 2.42), and for calculating the streamfunctions by inverting the vorticity (Equation 2.39). Figure 9 shows the grid convergence of the buoyancy derivative stencils when applied

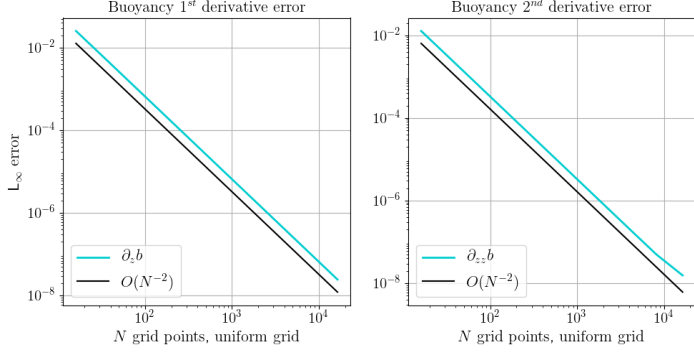


FIGURE 9. Grid convergence of buoyancy derivatives.

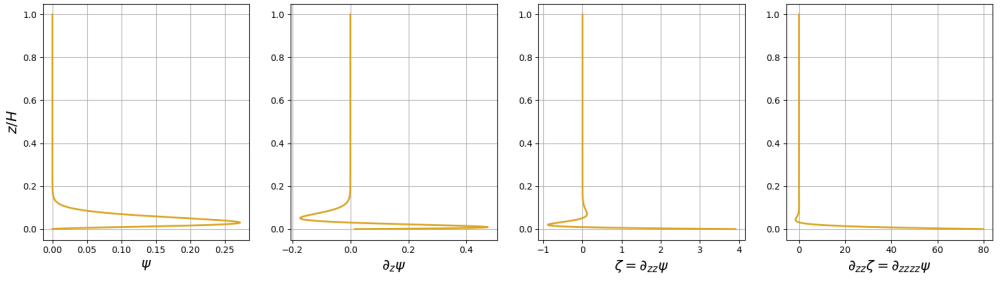
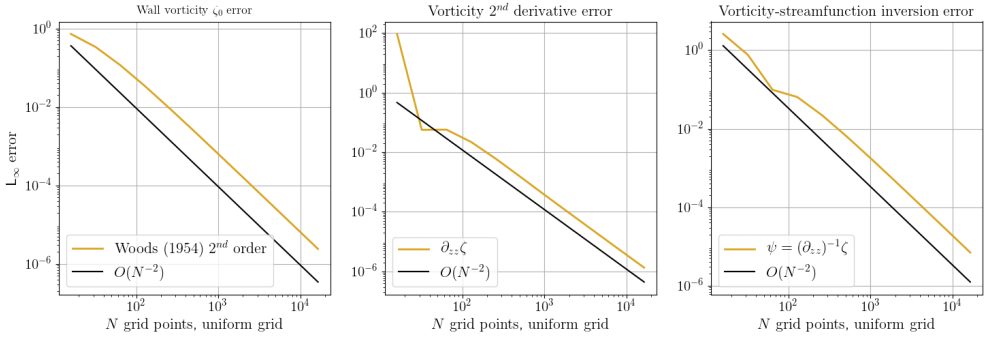

 FIGURE 10. Test function for ψ .


FIGURE 11. Grid convergence of finite differences for the vorticity.

to the test function $b = \cos(2\pi z/H)$. The test function for checking the inversions and vorticity derivatives,

$$\psi(z) = ((z+1)^3 - z^2 - 3z - 1)e^{-mHz} \quad (\text{C1})$$

was chosen because it satisfies the same boundary conditions as were required for the Floquet analysis. The test $\psi(z)$ is shown in Figure 10. The grid convergence of the Woods (1954) vorticity boundary condition (which imposes no-slip and impermeable boundary conditions on the diffusion of vorticity), the second derivative of vorticity, and the inversion of vorticity to obtain the streamfunction are shown in Figure 11.

Appendix D. Stokes' second problem governing equations

The governing equation for the spanwise vorticity disturbances are

$$\partial_t \zeta_2 = \underbrace{\frac{(\partial_{zz} - k^2)}{2}}_{\text{diffusion}} \zeta_2 - \underbrace{\frac{UikRe}{2}}_{\text{mean advection}} \zeta_2 + \underbrace{\frac{(\partial_{zz}U)ikRe}{2}}_{\text{vorticity line tilting by mean flow}} \psi + \underbrace{C^2(\partial_z - ik \cot \theta)}_{\text{baroclinic production of vorticity}} b, \quad (\text{D1})$$

and the governing equation for the buoyancy disturbances in the $x - z$ plane are

$$\partial_t b = \underbrace{\frac{(\partial_{zz} - k^2)}{2Pr}}_{\text{diffusion}} b - \underbrace{\frac{UikRe}{2}}_{\text{mean advection}} b + \underbrace{\frac{(\partial_z B)ikRe}{2}}_{\text{advection of mean buoyancy}} \psi. \quad (\text{D2})$$

Equation D2 and the baroclinic vorticity term in Equation D1 are eliminated for Stokes' second problem, where $C = 0$ and $b(z, t) = 0$. The remaining spanwise vorticity disturbance equation (Blennerhassett & Bassom (2006)) was used to calculate the linear stability of Stokes' second problem shown in Figure 4.

REFERENCES

- BAIDULOV, V. 2010 Fine structure of one-dimensional periodic stratified flows. *Fluid Dynamics* **45** (6), 835–842.
- BARKLEY, D. & HENDERSON, R. 1996 Three-dimensional floquet stability analysis of the wake of a circular cylinder. *Journal of Fluid Mechanics* **322**, 215–241.
- BÉNARD, H. & AVSEC, D. 1938 Travaux récents sur les tourbillons cellulaires et les tourbillons en bandes. applications à l'astrophysique et à la météorologie. *J. Phys. Radium* **9** (11), 486–500.
- BLENNERHASSETT, P. & BASSOM, A. 2002 The linear stability of flat stokes layers. *Journal of Fluid Mechanics* **464**, 393–410.
- BLENNERHASSETT, P. & BASSOM, A. 2006 The linear stability of high-frequency oscillatory flow in a channel. *Journal of Fluid Mechanics* **556**, 1–25.
- BRUNT, D. 1951 Experimental cloud formation. In *Compendium of Meteorology*, pp. 1255–1262. Springer.
- CHANDRA, K. 1938 Instability of fluids heated from below. *Proceedings of the Royal Society of London. Series A-Mathematical and Physical Sciences* **164** (917), 231–242.
- CHANT, R. & STONER, W. 2001 Particle trapping in a stratified flood-dominated estuary. *Journal of Marine Research* **59** (1), 29–51.
- DAUXOIS, T. & YOUNG, W. 1999 Near-critical reflection of internal waves. *Journal of Fluid Mechanics* **390**, 271–295.
- DAVIS, S. 1976 The stability of time-periodic flows. *Annual Review of Fluid Mechanics* **8** (1), 57–74.
- DEARDORFF, J. 1965 Gravitational instability between horizontal plates with shear. *The Physics of Fluids* **8** (6), 1027–1030.
- DELL, R. & PRATT, L. 2015 Diffusive boundary layers over varying topography. *Journal of Fluid Mechanics* **769**, 635–653.
- DWOYER, D. & HUSSAINI, M. 1987 *Stability of time dependent and spatially varying flows*. Springer.
- FERRARI, R., MASHAYEK, A., MCDUGALL, T., NIKURASHIN, M. & CAMPIN, J. 2016 Turning ocean mixing upside down. *Journal of Physical Oceanography*.
- FLOQUET, G. 1883 Sur les équations différentielles linéaires à coefficients périodiques. In *Annales scientifiques de l'École normale supérieure*, vol. 12, pp. 47–88.
- GALLAGHER, A. & MERCER, A. MCD 1965 On the behaviour of small disturbances in plane couette flow with a temperature gradient. *Proceedings of the Royal Society of London. Series A. Mathematical and Physical Sciences* **286** (1404), 117–128.

- GAYEN, B. & SARKAR, S. 2011 Direct and large-eddy simulations of internal tide generation at a near-critical slope. *Journal of Fluid Mechanics* **681**, 48–79.
- GEYER, R. & MACCREADY, P. 2014 The estuarine circulation. *Annual review of fluid mechanics* **46**, 175–197.
- GOFF, J. & ARBIC, B. 2010 Global prediction of abyssal hill roughness statistics for use in ocean models from digital maps of paleo-spreading rate, paleo-ridge orientation, and sediment thickness. *Ocean Modelling* **32** (1).
- HART, J. 1971 A possible mechanism for boundary layer mixing and layer formation in a stratified fluid. *Journal of Physical Oceanography* **1**, 258–262.
- HU, H. & KELLY, R. 1997 Stabilization of longitudinal vortex instabilities by means of transverse flow oscillations. *Physics of Fluids* **9** (3), 648–654.
- INGERSOLL, A. 1966 Convective instabilities in plane couette flow. *The Physics of Fluids* **9** (4), 682–689.
- IOOSS, G. & JOSEPH, D. 2012 *Elementary stability and bifurcation theory*. Springer Science & Business Media.
- JAYNE, S. & ST. LAURENT, L. 2001 Parameterizing tidal dissipation over rough topography. *Geophysical Research Letters* **28** (5), 811–814.
- KAISER, BRYAN EDWARD 2020 Finescale abyssal turbulence: sources and modeling. PhD thesis, Massachusetts Institute of Technology.
- KOVACIC, I., RAND, R. & SAH, S.M. 2018 Mathieu's equation and its generalizations: Overview of stability charts and their features. *Applied Mechanics Reviews* **70** (2).
- LORKE, A., PEETERS, F. & WÜEST, A. 2005 Shear-induced convective mixing in bottom boundary layers on slopes. *Limnology and Oceanography* **50** (5), 1612–1619.
- LORKE, A., UMLAUF, L. & MOHRHOLZ, V. 2008 Stratification and mixing on sloping boundaries. *Geophysical Research Letters* **35** (14).
- LUO, J. & WU, X. 2010 On the linear instability of a finite stokes layer: instantaneous versus floquet modes. *Physics of Fluids* **22** (5), 054106.
- NOACK, B. & ECKELMANN, H. 1994 A global stability analysis of the steady and periodic cylinder wake. *Journal of Fluid Mechanics* **270**, 297–330.
- PEACOCK, T., STOCKER, R. & ARISTOFF, J. 2004 An experimental investigation of the angular dependence of diffusion-driven flow. *Physics of Fluids* **16** (9), 3503–3505.
- PELTIER, W. & CAULFIELD, C. 2003 Mixing efficiency in stratified shear flows. *Annual Review of Fluid Mechanics* **35** (1), 135–167.
- PHILLIPS, O. 1970 On flows induced by diffusion in a stably stratified fluid. *Deep Sea Research and Oceanographic Abstracts* **17** (3), 435–443.
- RAPAKA, N., GAYEN, B. & SARKAR, S. 2013 Tidal conversion and turbulence at a model ridge: direct and large eddy simulations. *Journal of Fluid Mechanics* **715**, 181–209.
- ROBICHAUX, J., BALACHANDAR, S. & VANKA, S. 1999 Three-dimensional floquet instability of the wake of square cylinder. *Physics of Fluids* **11** (3).
- SARKAR, S. & SCOTTI, A. 2017 From topographic internal gravity waves to turbulence. *Annual Review of Fluid Mechanics* **49**, 195–220.
- SIMPSON, J., BROWN, J., MATTHEWS, J. & ALLEN, G. 1990 Tidal straining, density currents, and stirring in the control of estuarine stratification. *Estuaries* **13** (2), 125–132.
- TREFETHEN, LLOYD N, TREFETHEN, ANNE E, REDDY, SATISH C & DRISCOLL, TOBIN A 1993 Hydrodynamic stability without eigenvalues. *Science* **261** (5121), 578–584.
- VON KERCZEK, C. & DAVIS, S. 1976 The instability of a stratified periodic boundary layer. *Journal of Fluid Mechanics* **75** (2), 287–303.
- WOODS, L. 1954 A note on the numerical solution of fourth order differential equations. *The Aeronautical Quarterly* **5** (4), 176–184.
- WUNSCH, C. 1970 On oceanic boundary mixing. *Deep Sea Research and Oceanographic Abstracts* **17** (2), 293–301.
- ZILBERMAN, N., BECKER, J., MERRIFIELD, M. & CARTER, G. 2009 Model estimates of m 2 internal tide generation over mid-atlantic ridge topography. *Journal of Physical Oceanography* **39** (10), 2635–2651.